Integrated hepatic ferroptosis gene signature dictates pathogenic features of ferroptosis

VISUAL ABSTRACT

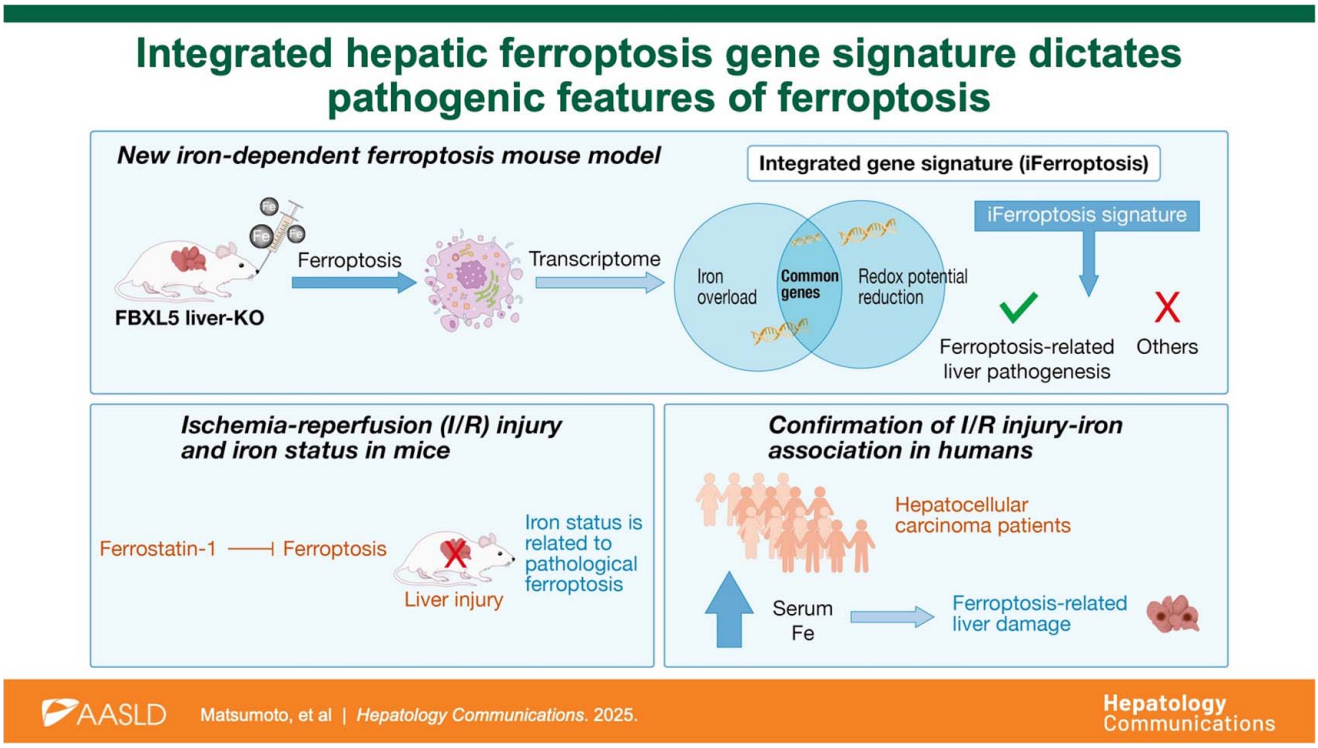

AASLD Matsumoto, et al | *Hepatology Communications*. 2025. Hepatology Communications

Received: 15 November 2024 | Accepted: 19 March 2025

DOI: 10.1097/HC9.0000000000000721

ORIGINAL ARTICLE

OPEN

Integrated hepatic ferroptosis gene signature dictates pathogenic features of ferroptosis

Takashi Matsumoto[1,2] | **Akihiro Nita**[3] | **Yohei Kanamori**[1] | **Ayato Maeda**[1] | **Tomomi Nita**[1] | **Noriko Yasuda-Yoshihara**[2,4] | **Kosuke Mima**[2] | **Hirohisa Okabe**[2] | **Katsunori Imai**[2] | **Hiromitsu Hayashi**[2] | **Yuta Matsuoka**[5] | **Katsuya Nagaoka**[6] | **Keiichi I. Nakayama**[7,8] | **Yuki Sugiura**[5] | **Yasuhito Tanaka**[6,9] | **Hideo Baba**[2,9] | **Toshiro Moroishi**[1,3,9]

[1]Department of Molecular and Medical Pharmacology, Faculty of Life Sciences, Kumamoto University, Kumamoto, Japan

[2]Department of Gastroenterological Surgery, Graduate School of Medical Sciences, Kumamoto University, Kumamoto, Japan

[3]Division of Cellular Dynamics, Medical Research Laboratory, Institute of Integrated Research, Institute of Science Tokyo, Tokyo, Japan

[4]R&D Laboratory for Innovative Biotherapeutics, Graduate School of Pharmaceutical Sciences, Kyushu University, Fukuoka, Japan

[5]Center for Cancer Immunotherapy and Immunobiology, Kyoto University Graduate School of Medicine, Kyoto, Japan

[6]Department of Gastroenterology and Hepatology, Faculty of Life Sciences, Kumamoto University, Kumamoto, Japan

[7]Anticancer Strategies Laboratory, Advanced Research Initiative, Institute of Integrated Research, Institute of Science Tokyo, Tokyo, Japan

[8]Department of Molecular and Cellular Biology, Medical Institute of Bioregulation, Kyushu University, Fukuoka, Japan

[9]Center for Metabolic Regulation of Healthy Aging, Faculty of Life Sciences, Kumamoto University, Kumamoto, Japan

Correspondence
Toshiro Moroishi, Division of Cellular Dynamics, Medical Research Laboratory, Institute of Integrated Research, Institute of Science Tokyo, 1-5-45 Yushima, Bunkyo-ku, Tokyo 113-8510, Japan.
Email: moroishi.toshiro@tmd.ac.jp

Abstract

Background: Ferroptosis, a distinctive form of cell death induced by iron-dependent lipid peroxidation, is implicated in various biological processes, including liver diseases. Establishing an iron overload-induced ferroptosis model and identifying hepatic gene signatures associated with ferroptosis are crucial for understanding its role in liver pathogenesis.

Methods: F-box and leucine-rich repeat protein 5 (FBXL5) is a substrate-recognition component of the SCF E3 ligase complex that restricts intracellular iron levels. In this study, we used liver-specific *Fbxl5*-null mice to establish an iron overload-induced ferroptosis model. Transcriptome

Abbreviations: 4-HNE, 4-hydroxynonenal; ACSL4, acyl-CoA synthetase long chain family member 4; ACTB, actin beta; ALBI, albumin–bilirubin; APAP, acetaminophen; CCL4, carbon tetrachloride4; DDBJ, DNA Data Bank of Japan; DEGs, differentially expressed genes; FAC, ferric ammonium citrate; FBXL5, F-box and leucine-rich repeat protein 5; FGF21, fibroblast growth factor 21; GDF15, growth differentiation factor 15; GPX4, glutathione peroxidase 4; GSEA, gene set enrichment analysis; H&E, hematoxylin and eosin; HIRI, hepatic ischemia-reperfusion injury; HMOX1, heme oxygenase 1; HRMS, high-resolution mass spectrometry; ICGR15, indocyanine green retention 15; IER2, immediate early response2; IRP1, iron regulatory protein 1; IRP2, iron regulatory protein 2; KEGG, Kyoto Encyclopedia of Genes and Genomes; KO, knockout; LC/HRMS, liquid chromatography coupled with HRMS; LDH, lactate dehydrogenase; MALDI–MS/MS/MSI, matrix-assisted laser desorption/ionization–tandem MS–MS imaging; MS/MS, tandem mass spectrometry; NES, normalized enrichment score; OCT, optimal cutting temperature; PC, phosphatidylcholine; PUFA, polyunsaturated fatty acid; qPCR, quantitative polymerase chain reaction; RT, reverse transcription; TfR1, transferrin receptor 1.

Toshiro Moroishi—Lead contact.

Supplemental Digital Content is available for this article. Direct URL citations are provided in the HTML and PDF versions of this article on the journal's website, www.hepcommjournal.com.

analysis identified genes involved in hepatic ferroptosis. Integrating these gene signatures with another ferroptosis model enabled the assessment of ferroptosis-related pathology in murine liver injury models and in 174 patients undergoing liver resection surgery.

Results: Iron overload induced severe liver damage in liver-specific *Fbxl5*-null mice, characterized by elevated liver enzymes, histopathological changes, and lipid peroxidation. Transcriptome analysis revealed a distinct set of genes associated with hepatic ferroptosis response. Generating a gene signature for evaluating ferroptosis enhanced the understanding of ferroptosis-related pathologies in liver diseases. Iron overload exacerbated liver damage in murine ischemia-reperfusion injury models via ferroptosis induction. In human patients, elevated serum iron levels correlated with sustained postoperative liver damage, indicating heightened susceptibility to ferroptosis.

Conclusions: Here, a murine model of iron overload-induced hepatic ferroptosis was established, and a gene signature indicative of hepatic ferroptosis response in both mice and humans was identified. These findings underscore the role of ferroptosis in liver injury progression and suggest potential therapeutic targets for liver disease intervention.

Keywords: ferroptosis, gene signature, hepatectomy, ischemic reperfusion injury

INTRODUCTION

Ferroptosis is a distinct form of cell death that differs from previously described modes, such as apoptosis, necrosis, and necroptosis, as it is induced by iron-dependent lipid peroxidation.[1,2] Its morphological characteristics primarily include marked shrinkage of mitochondria, increased mitochondrial membrane density, and the reduction or disappearance of mitochondrial cristae.[3] Since its discovery, ferroptosis has been implicated in various biological contexts,[4] including aging,[5,6] neurodegenerative disorders,[7–9] infectious diseases,[10,11] autoimmune diseases,[12,13] and cancer.[14–16] Consistent with the broad biological impact of ferroptosis, emerging evidence indicates an association between ferroptosis and the pathogenesis of liver diseases, including liver injury, steatohepatitis, fibrosis, cirrhosis, and liver cancer.[17] In particular, hepatic ischemia-reperfusion injury (HIRI), which occurs during liver transplantation and liver resection surgery, poses a critical issue as it directly leads to postoperative graft dysfunction or remnant liver dysfunction.[18] HIRI primarily follows a biphasic mechanism consisting of an ischemic phase, caused by initial ischemia, and a reperfusion phase that occurs after the restoration of blood flow. During the ischemic phase, hepatocytes and non-parenchymal cells in the liver are exposed to hypoxic conditions, resulting in ATP depletion and mitochondrial dysfunction, which in turn trigger oxidative stress. In the reperfusion phase, the rapid restoration of oxygen supply leads to increased production of reactive oxygen species, further exacerbating oxidative stress.[19] Additionally, the activation of Kupffer cells induces the release of inflammatory cytokines, complement activation, and neutrophil infiltration, thereby amplifying tissue damage.[20] The widespread availability of next-generation sequencing data in the public domain has fueled interest in developing gene signatures to monitor hepatic ferroptosis, thereby elucidating its connection to liver disease pathogenesis and evaluating its potential as a target for prevention and treatment. However, this has been challenging, particularly when identifying gene signatures that dictate tissue-level responses, because of the limited options for animal models for inducing hepatic ferroptosis.

Excess iron within cells can induce the Fenton reaction, producing highly reactive hydroxyl radicals that oxidize phospholipids containing polyunsaturated fatty acids (PUFAs), leading to ferroptosis. Maintaining strict control over iron homeostasis and redox potential against oxidative stress is crucial for preventing ferroptosis, as imbalances can induce this form of cell death.[21] Ferroptosis can be initiated by a reduction in redox potential, such as the depletion of reduced glutathione and decreased activity of glutathione peroxidase 4 (GPX4). Consequently, glutathione depletion induced by an acetaminophen (APAP) overdose[22] and the conditional deletion of

GPX4 in the liver[23] are widely used methods to induce hepatic ferroptosis. Despite the critical role of iron in ferroptosis induction, an iron overload-induced hepatic ferroptosis model has not yet been established.

In mammals, iron exists in two oxidation states, ferrous iron (Fe^{2+}) and ferric iron (Fe^{3+}). Iron absorbed by cells is released into the cytosol in its ferrous form. Ferrous iron is either directly integrated into iron-dependent proteins or directed to the mitochondria, where it becomes part of heme and iron–sulfur clusters.[24] However, ferrous iron is redox-active and triggers the generation of reactive oxygen species. To mitigate its harmful effects, any unused or excess ferrous iron is converted into the ferric form and stored within ferritin.[25,26] Ferric iron is relatively safer in terms of oxidative damage, but must be reduced back to the ferrous state to enter the cellular bioavailable iron pool. Because of the distinct biological characteristics of ferrous and ferric iron, their valence states and quantities influence both biological and pathological outcomes related to iron. Ferrous iron is considered a potent inducer of ferroptosis. Cellular levels of ferrous iron are primarily regulated in vivo by F-box and leucine-rich repeat protein 5 (FBXL5).[27] FBXL5 is a substrate-recognition component of the SCF E3 ligase complex that mediates the ubiquitination and degradation of iron regulatory protein 1 (IRP1, also known as ACO1) and iron regulatory protein 2 (IRP2, also known as IREB2),[28,29] thus controlling intracellular ferrous iron levels by regulating the protein expression of iron metabolism-related components at the post-transcriptional level. We have previously reported that the loss of FBXL5 in mice results in embryonic lethality, whereas liver-specific *Fbxl5* ablation is associated with ferrous iron accumulation and mitochondrial dysfunction in hepatocytes, leading to steatohepatitis.[27] Additionally, when these mice were fed a high-iron diet, they died of acute liver failure due to excess iron. In the present study, we used this animal model to establish an iron overload-induced ferroptosis model and identify commonly regulated genes in the hepatic response to ferroptosis using a transcriptome-wide approach. We used this newly generated gene set to uncover the key functions of iron in the pathogenesis of HIRI in both mice and humans.

METHODS

Mice

Fbxl5$^{F/F}$ mice were generated as described previously.[27] These mice were crossed with *Alb*-Cre transgenic mice[30] to generate *Alb*-Cre/*Fbxl5*$^{F/F}$ mice. Age-matched (8–14 wk) and sex-matched littermates were used for the experiments. All mice were back-crossed with C57BL/6 mice for more than 7 generations under specific pathogen-free conditions. All mouse experiments were approved by the Animal Ethics Committee of Kumamoto University (A2021-061).

Patients data

Tissue specimens were obtained from patients with HCC who underwent hepatectomy at the Department of Gastroenterological Surgery, Kumamoto University Hospital, between April 2007 and October 2023 (n = 1014 patients). Patients were excluded if pre-operative serum iron levels were not measured (n = 840). Finally, 174 patients were retrospectively analyzed. For the data on ischemic time, 8 patients were excluded because the exact duration of hepatic ischemia performed using the Pringle maneuver method was not clear from the operation records, leaving 166 patients for final analysis. The present study was approved by the Medical Ethics Committee of Kumamoto University (Project numbers 1291 and 2107), and written informed consent was obtained from all participants. The specimens of the cancerous tissue and adjacent background tissue of the surgical resection specimen were collected as a single mass, embedded in an optimal cutting temperature (OCT) compound, quickly frozen on dry ice, and stored at −80 °C. The frozen specimens were sliced into 20-μm-thin sections, the background non-cancer areas were identified by H&E staining, and RNA from this area was separately extracted using the RNeasy mini kit (QIAGEN, Cat# 74104).

Iron administration

The animals were restrained by tight scruffing using a non-gavage hand. Oral gavage was performed using 1.5 inch, 20-gauge, stainless steel feeding needles with a 1.9 mm ball (Sigma-Aldrich, Cat# CAD9921), administering a final dose of 600 mg/kg of ferric ammonium citrate (FAC; Sigma-Aldrich, Cat# M0512) in 15 mL/kg of gavage solution. The gavage solution consisted of a mixture of 67% olive oil (Fujifilm, Cat# 150-00276) and 33% water containing 120 mg/mL of FAC (resulting in a final concentration of 40 mg/mL FAC in the gavage solution). A vehicle solution comprising 67% olive oil and 33% water was used as the control. For mass spectrometry experiments, the mice were administered a final dose of 1500 mg/kg FAC via oral gavage. Iron gavage was administered after 12–16 hours of fasting. For damage prevention experiments, the ferroptosis inhibitor ferrostatin-1 (Fer-1; Cayman Chemical, Cat# 17729) was dissolved in a vehicle buffer containing 10% DMSO (Fujifilm, Cat# 046-21981), 45% polyethylene glycol 300 (PEG300; Selleck, Cat# S6704), and 45% PBS. Fer-1 solution or vehicle was administered intraperitoneally 1 hour before the oral gavage experiment.

Liquid chromatography-high resolution tandem mass spectrometry analysis of oxidized phosphatidylcholine

Liquid chromatography-high resolution tandem mass spectrometry (LC–MS/MS) analysis was performed using a Nexera LC system (Shimadzu Corp.) coupled with a high-performance benchtop quadrupole Orbitrap mass spectrometer (Q Exactive; Thermo Fisher Scientific) equipped with an electrospray ionization source. The LC parameters, ionization conditions, and experimental conditions for MS/MS and parallel reaction monitoring have been described previously.[31] LC–HRMS/MS analysis was performed using Xcalibur 4.2.47 software (Thermo Fisher Scientific).

Matrix-assisted laser desorption/ionization–tandem MS–MS imaging of oxidized lipids

Sample preparation for matrix-assisted laser desorption/ionization–tandem MS–MS imaging (MALDI–MS/MS/MSI) was performed as described previously.[31] Briefly, thin liver sections (8 μm) were prepared using a cryomicrotome (CM3050; Leica Microsystems) and mounted on indium tin oxide-coated glass slides (Bruker Daltonics GmbH). The slides were coated with 2,5-dihydroxybenzoic acid solution (50 mg/mL in 80% aqueous ethanol) by manual spraying using an artistic brush (Procon Boy FWA Platinum; Mr. Hobby). MALDI-MS/MS and MALDI-MSI experiments were performed using a MALDI linear ion trap mass spectrometer (MALDI LTQ XL; Thermo Fisher Scientific) equipped with a 60-Hz N2 laser ($\lambda = 337$ nm). The laser energy and the raster step size were set at 32 μJ and 60 μm, respectively. Auto-gain control (in which the ion trap is filled with the optimum number of ions) was not utilized in this experiment. Mass spectra were acquired in positive ion mode, and MS/MS transitions for phosphatidylcholine (PC) PUFA; $^{18}O_2$ imaging were as follows: m/z 794.5 → 774.5 (neutral loss of $H_2^{18}O$) for PC34:2; $^{18}O_2$ with a precursor ion isolation width of m/z 1.0. After sample analysis, ion images were reconstructed using the ImageQuest v. 1.0.1 software (Thermo Fisher Scientific).

Mouse models for HIRI

Mice were fasted for 12–16 hours prior to the operation, followed by anesthesia with medetomidine (10 mg/kg), midazolam (50 mg/kg), and butorphanol (50 mg/kg) via i.p. injection. A midline incision was made, and an atraumatic clip was placed across the portal vein, hepatic artery, and bile duct just above the right branch. This procedure interrupts blood flow to the left lateral and median lobes, representing ~70% of the total blood supply to the liver. After 30 minutes of partial hepatic ischemia, the clip was removed to initiate reperfusion. Sham mice underwent the same procedure without vascular occlusion. After 3 hours of reperfusion, the mice were euthanized via exsanguination under anesthesia, and serum samples were collected. The left lateral and median lobes of the liver were collected and immediately fixed in 4% phorbol myristate acetate and stored at −80 °C until further analysis. For damage prevention experiments, Fer-1 was dissolved in vehicle buffer containing 10% DMSO, 45% PEG300, and 45% PBS. Fer-1 solution or vehicle was administered intraperitoneally 1 hour before HIRI.

Immunoblot analysis

Total protein extracts were prepared from mouse liver by lysis with a solution comprising 50 mM Tris–HCl (pH 7.5), 150 mM NaCl, 0.5% Triton X-100, aprotinin (10 μg/mL), leupeptin (10 μg/mL), 1 mM phenylmethylsulfonyl fluoride, 400 μM Na3VO4, 400 μM EDTA, 10 mM NaF, and 10 mM sodium pyrophosphate. The extracts (40 μg of protein) were fractionated by SDS–PAGE on a 10% gel, and the separated proteins were then transferred to a polyvinylidene difluoride membrane (Millipore, Cat# IPVH00010). The membrane was exposed to 3% dried skim milk and then incubated overnight at 4 °C with primary antibodies against transferrin receptor protein 1 (TfR1; Thermo Fisher Scientific, Cat# 13-6800), IRP2 (Millipore, Cat# MABS2030-100UG), or actin (ACTB; Cell Signaling Technology, Cat# 12620). Immune complexes were detected with HRP-conjugated secondary antibodies and enhanced chemiluminescence reagents.

Reverse transcription and real-time PCR analysis

Total RNA was isolated from the liver using ISOGEN (NIPPON GENE, Cat# 319-90211) and reverse-transcribed to complementary DNA (cDNA) using PrimeScript RT Master Mix (Takara, Cat# RR036A). The cDNA was then diluted and used for quantification by performing real-time PCR in a StepOnePlus Real-Time PCR System (Thermo Fisher Scientific) with the SYBR Premix Ex Taq II kit (Takara, Cat# RR820). The PCR primers used were as follows:

RNA sequencing and data analysis

Total RNA was extracted from the livers of fasting mice using TRIzol (Life Technologies, Cat# 15596-018) according to the manufacturer's instructions. The RNA was then subjected to sequencing using an Illumina NovaSeq. 6000 sequencer (2 × 150 bp read length). The quality of the raw paired-end reads was assessed using FastQC (version v0.12.1), and adaptor

sequences were trimmed using Trim Galore (version 0.6.10). Paired-end reads were mapped against mouse (GRCm39) or human (GRCh38) genomes and analyzed using a series of programs, including HISAT2 (version 2.1.1), featureCounts (version 2.16.1), and DESeq. 2 (version 1.42.1). The expression data were further analyzed using GSEA v4.1.0 software. Gene sets for gene set enrichment analysis (GSEA) were obtained from the Molecular Signatures Database v4.0, which is available on the GSEA website. Raw RNA-seq data, supporting the findings of the present study, are available from the DNA Data Bank of Japan [DDBJ; accession numbers PRJDB18097 (mouse data) and PRJDB18207 (human data)].

GSEA

The expression data were analyzed using GSEA v4.1.0 software. Gene sets for GSEA were obtained from the Molecular Signatures Database v4.0. The RNA sequencing data used for each figure are as follows: Figure 3D, RNA sequencing data was obtained from GSE117066,[32] comparing normal group (n = 3, indicated as control) and ischemic reperfusion group (n = 3, subjected to 70% hepatic ischemic reperfusion); Figure 3E, RNA sequencing data was obtained from Li et al,[33] comparing methionine–choline-deficient diet group (n = 3) and normal diet group (n = 3); Figure 3F: RNA sequencing data was obtained from GSE207855,[34] comparing control group (n = 6) and carbon tetrachloride (CCl_4) injection group (n = 6); Figure 4E: RNA sequencing data was obtained from GSE113024,[35] comparing donor liver at the end of preservation in conventional liver transplantation group (n = 3) and post-reperfusion group (n = 3).

Histopathology and immunostaining

Histological analysis was performed as previously described,[27] with slight modifications. Briefly, liver samples were fixed with 4% paraformaldehyde in PBS, embedded in paraffin, sectioned using a microtome, and stained with hematoxylin and eosin (H&E) according to standard protocols. For Perls Prussian blue staining to detect iron, deparaffinized and hydrated liver sections were incubated for 30 minutes at room temperature with Perls reagent (5% potassium ferrocyanide and 5% hydrogen chloride in deionized water) and then counterstained with hematoxylin solution for 30 seconds. For immunostaining analysis, deparaffinized and hydrated liver sections underwent antigen retrieval using HISTOFINE antigen retrieval solution (Nichirei, Cat# 415201). Tissues were then stained with antibodies against 4-hydroxynonenal (4-HNE; Abcam, Cat# ab46545) according to standard procedures and counterstained with hematoxylin solution for 30 seconds. Sections from control and mutant mice were processed simultaneously to monitor and detect nonspecific staining.

Statistical analysis

All data were analyzed using GraphPad Prism (GraphPad Software). mRNA analysis was performed using a base 10 logarithm transformation. Statistical parameters and methods are detailed in the figure legends. Statistical significance was defined as a p value < 0.05.

RESULTS

Establishment of an iron overload-induced ferroptosis model using liver-specific *Fbxl5*-null mice

We generated mice with liver-specific ablation of *Fbxl5* by crossing *Fbxl5*$^{F/F}$ mice, carrying floxed *Fbxl5* alleles, with *albumin (Alb)*-Cre transgenic mice (expressing Cre recombinase under the regulation of the *Alb* promoter). Consistent with previous results,[27] almost all floxed alleles were inactivated by Cre recombinase in the liver of *Alb-Cre*/*Fbxl5*$^{F/F}$ mice, as evidenced by a corresponding decrease in the amount of *Fbxl5* mRNA (Supplemental Figure S1A, http://links.lww.com/HC9/B994). Immunoblot analysis revealed that IRP2 accumulated in the liver of these mice, which was associated with an increased expression of transferrin receptor 1 (TfR1, also known as TFRC), a downstream target of IRP2 (Supplemental Figure S1B, http://links.lww.com/HC9/B994). To establish an iron overload-induced liver ferroptosis model, we conducted oral iron gavage experiments using liver-specific FBXL5-deficient [*Alb-Cre*/*Fbxl5*$^{F/F}$; referred to as FBXL5 liver-KO (knockout)] mice and *Fbxl5*$^{F/F}$ control mice (Figure 1A). Although iron administration had minimal impact on control mice, the serum levels of AST, ALT, and lactate dehydrogenase (LDH) dramatically increased in FBXL5 liver-KO mice at 3 and 6 hours after administration (Figure 1B). Consistent with these results, microscopic analysis of H&E-stained sections demonstrated increased hepatocyte damage in the livers of FBXL5 liver-KO mice (Figure 1C). Perls iron staining further demonstrated increased iron accumulation in the hepatocytes of FBXL5 liver-KO mice compared to control mice (Figure 1D). Immunostaining of 4-HNE–modified proteins indicated a marked increase in lipid peroxidation (Figure 1E). Indeed, LC–HRMS/MS analysis of oxidized PC revealed a marked increase in single, double, and triple oxygenated PC PUFA levels (PC PUFA; O/O2/O3), characteristic of ferroptosis induction,[36] in the livers of FBXL5 liver-KO mice compared to that in control mice upon iron

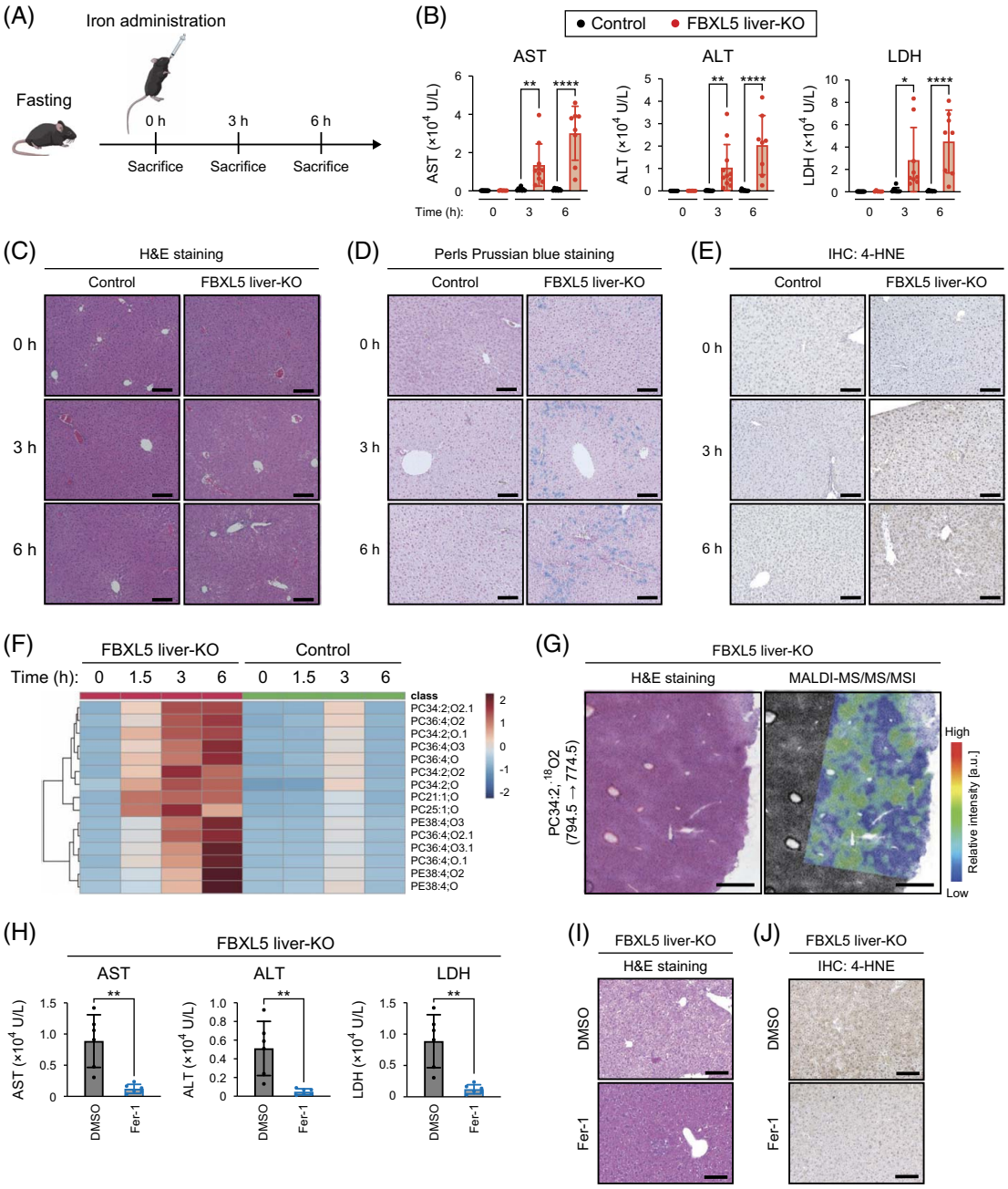

FIGURE 1 Establishment of an iron overload-induced ferroptosis model using liver-specific *Fbxl5*-null mice. (A) Schematic overview of the experimental procedure for ferroptosis induction. (B) Serum levels of AST, ALT, and LDH in *Fbxl5*$^{F/F}$ (control) and *Alb*-Cre/*Fbxl5*$^{F/F}$ (FBXL5 liver-KO) mice at the indicated times after iron administration. Data are represented as mean ± SD. The number of mice used for this data are as follows: AST, n = 12, 8, and 7 mice at 0, 3, and 6 hours, respectively, for the control group; and n = 6, 10, and 8 mice at 0, 3, and 6 hours, respectively, for the FBXL5 liver-KO group; ALT, n = 12, 11, and 10 mice at 0, 3, and 6 hours, respectively, for the control group; and n = 6, 11, 8 mice at 0, 3, 6 hours, respectively, for the FBXL5 liver-KO group; LDH, n = 12, 9, and 7 mice at 0, 3, and 6 hours, respectively, for the control group; and n = 6, 9, and 8 mice at 0, 3, and 6 hours, respectively, for the FBXL5 liver-KO group. $*p < 0.05$; $**p < 0.01$; $****p < 0.0001$ (one-way ANOVA test followed by the Tukey multiple comparison test). (C–E) Histological analysis of the liver of *Alb*-Cre/*Fbxl5*$^{F/F}$ (FBXL5 liver-KO) mice compared with that of *Fbxl5*$^{F/F}$ (control) mice. H&E staining is shown in (C), Perls Prussian blue staining for the detection of iron is shown in (D), and IHC staining with antibodies against 4-HNE is shown in (E). Scale bars represent 100 μm. (F) Heatmap showing time-dependent profiles of endogenous oxidized phosphatidylcholines in lipid extracts from the liver of *Fbxl5*$^{F/F}$ (control) and *Alb*-Cre/*Fbxl5*$^{F/F}$ (FBXL5 liver-KO) mice at the indicated times after iron administration. The color reflects the normalized MS peak area of each oxidized phosphatidylcholines using $\log_{10}$ transformation and autoscaling. (G) Histological analysis of the liver of *Alb*-Cre/*Fbxl5*$^{F/F}$ (FBXL5 liver-KO) mice was conducted at 3 hours after iron administration. The H&E staining results are shown in the left panel, and the MALDI–MS/MS/MSI results for PC34:2; $^{18}O_2$ (794.5 → 774.5) are demonstrated in the right panel. Scale bars represent 500 μm. (H) Serum levels of AST, ALT, and LDH in *Alb*-Cre/*Fbxl5*$^{F/F}$ (FBXL5 liver-KO) mice provided (or not) with the ferroptosis inhibitor ferrostatin-1 (Fer-1) for 1 hour prior to iron exposure for 3 hours. Data are represented as mean ± SD; n = 6 mice for each group. $**p < 0.01$ (unpaired *t* test). (I and J) Histological analysis of the liver of *Alb*-Cre/*Fbxl5*$^{F/F}$ (FBXL5 liver-KO) mice treated as in (H). H&E staining is shown in (I), and IHC staining with antibodies against 4-HNE is shown in (J). Scale bars represent 100 μm.

Abbreviations: 4-HNE, 4-hydroxynonenal; ischemia-reperfusion injury; FBXL5, F-box and leucine-rich repeat protein 5; H&E, hematoxylin and eosin; IHC, immunohistochemical; KO, knockout; LDH, lactate dehydrogenase; MALDI–MS/MS/MSI, matrix-assisted laser desorption/ionization–tandem MS–MS imaging; MS, mass spectrometry.

administration (Figure 1F). To investigate the association between oxidized PC PUFAs and hepatic cell death, we conducted in vivo ^{18}O stable isotope labeling and MALDI–MS/MS/MSI to visualize endogenous oxidized PC PUFAs.[31] FBXL5 liver-KO mice were exposed to a flow of $^{18}O_2$ air for 3 hours after iron administration. Subsequent analysis revealed significant accumulation of doubly oxygenated PC PUFAs, specifically PC34:2; $^{18}O_2$, in the damaged liver areas of FBXL5 liver-KO mice (Figure 1G), suggesting an association between oxidized PC PUFA accumulation and liver damage induced by iron administration in these mice. Altogether, these observations suggest that iron administration leads to the massive accumulation of lipid peroxidation in the livers of FBXL5 liver-KO mice. To confirm that iron-induced hepatotoxicity in FBXL5 liver-KO mice was due to ferroptosis, we intraperitoneally injected Fer-1, a ferroptosis inhibitor, before iron administration. Treatment with Fer-1 reduced the levels of liver transaminases and LDH (Figure 1H), histopathological liver damage (Figure 1I), and levels of 4-HNE–modified proteins (Figure 1J) compared to control DMSO treatment. Therefore, we established an in vivo mouse model of iron overload-induced ferroptosis by administering iron to FBXL5 liver-KO mice.

Liver-specific FBXL5 deficiency induces unique gene expression profiles upon iron administration

To investigate the changes in the liver transcriptome induced by ferroptosis, we examined the time-dependent gene expression profiles in the livers of FBXL5 liver-KO mice and control mice following iron administration (Figure 2A and Supplemental Table S1, http://links.lww.com/HC9/B985). Principal component analysis (Figure 2B) and a heatmap of differentially expressed genes (DEGs) (Figure 2C) revealed extensive alterations in the liver transcriptome of FBXL5 liver-KO mice at 3 and 6 hours after iron administration. To investigate the immediate effects of ferroptosis on liver tissue response, we compared the gene expression patterns between FBXL5 liver-KO mice and control mice 3 hours after iron administration (Supplemental Table S2, http://links.lww.com/HC9/B986). GSEA highlighted the enrichment of ferroptosis-related gene set (mmu04216) in the livers of FBXL5 liver-KO mice (Figure 2D), indicating the induction of ferroptosis. These findings collectively demonstrate that our mouse model of iron overload-induced ferroptosis can effectively replicate the pathogenesis of ferroptosis in vivo, characterized by both histological changes and alterations in gene expression profiles.

Integrated ferroptosis response gene signature dictates ferroptosis-related pathological response in mouse liver

Ferroptosis, induced by an imbalance between iron toxicity and antioxidants, can also be influenced by a reduction in redox potential.[21] Among such mouse models, APAP overdose-induced glutathione depletion serves as a widely used mouse model for ferroptosis induction in the liver.[22] To better understand the hepatic gene signature indicative of ferroptosis induction in vivo, we aimed to narrow down the gene list obtained from our iron overload-induced ferroptosis model by comparing it with that from the APAP-induced ferroptosis model. First, we characterized the genes whose expressions are commonly altered in APAP overdose-induced and iron overload-induced ferroptosis models (Figure 3A). Reanalysis of gene expression data from Li et al[32] identified 479 DEGs (220 and 259 genes with upregulated and downregulated expressions, respectively) (Supplemental Table S3, http://links.lww.com/HC9/B987) in the livers of APAP-treated mice compared to those in control mice (Figure 3B, left). Furthermore, RNA sequencing analysis identified 1242 DEGs (733 and 509 genes with upregulated and downregulated expressions, respectively) (Supplemental Table S4, http://links.lww.com/HC9/B988) in the livers of FBXL5 liver-KO mice at 0 and 3 hours after iron administration (Figure 3B, right). Given that only 33 genes, including 14 unannotated genes, were similarly downregulated in both APAP overdose-induced and iron overload-induced ferroptosis models, we focused on genes commonly upregulated in both models. The top 100 genes with upregulated expressions common to both models were selected to establish a gene set termed the “integrated gene signature for hepatic ferroptosis response (iFerroptosis)” (Figure 3C and Supplemental Table S5, http://links.lww.com/HC9/B989). Next, we investigated whether the iFerroptosis gene set could better characterize the pathological features of ferroptosis in the mouse liver than the existing gene set for ferroptosis (mmu04216). We applied the iFerroptosis gene list to the liver transcriptome of HIRI (Supplemental Table S6, http://links.lww.com/HC9/B990),[37] and CCl_4-induced acute liver injury (Supplemental Table S7, http://links.lww.com/HC9/B991).[34]

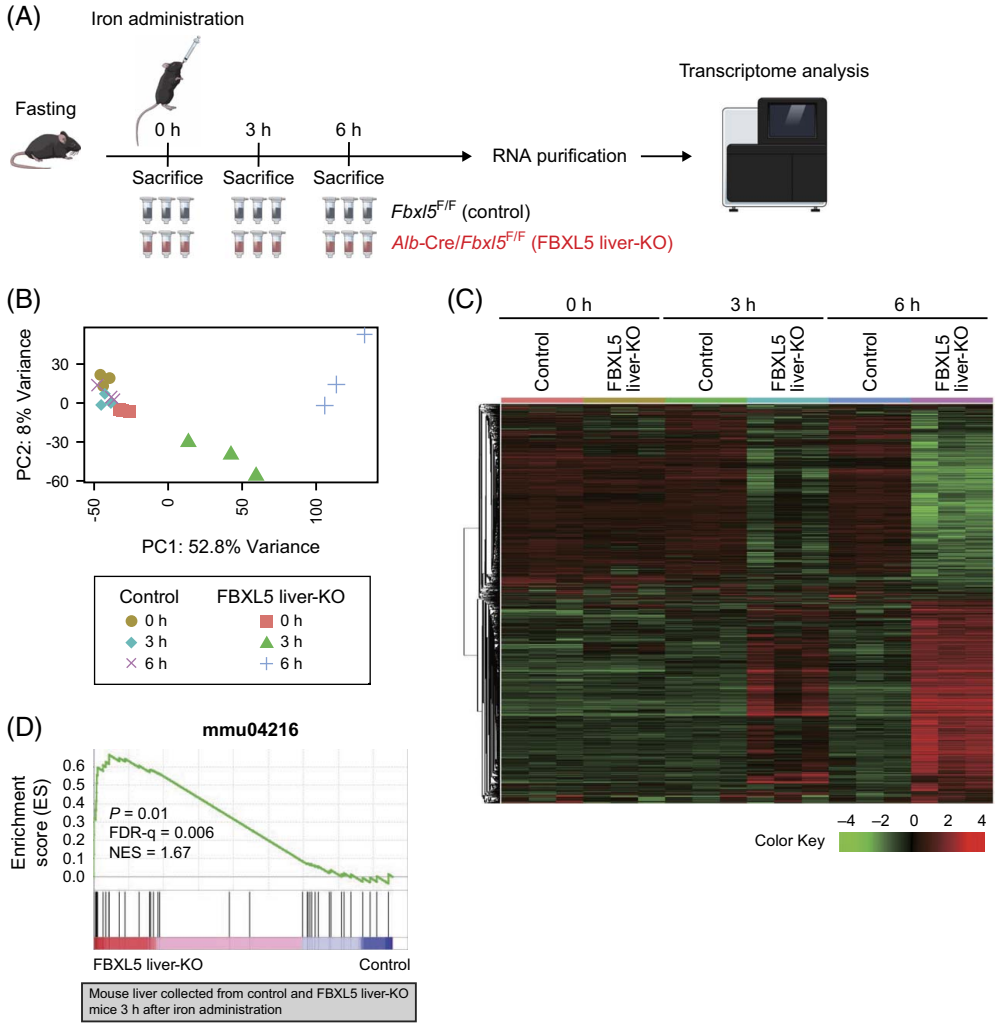

FIGURE 2 Characterization of the gene expression profiles of the liver in response to iron overload-induced ferroptosis. (A) Schematic overview of sample preparation for the transcriptome analysis. (B) Principal component analysis of the transcriptome of the liver of *Fbxl5*$^{F/F}$ (control) and *Alb*-Cre/*Fbxl5*$^{F/F}$ (FBXL5 liver-KO) mice at the indicated times after iron administration. (C) Heatmap correlation of *Fbxl5*$^{F/F}$ (control) and *Alb*-Cre/*Fbxl5*$^{F/F}$ (FBXL5 liver-KO) mice at the indicated times after iron administration. (D) Gene set enrichment analysis (GSEA) of the Kyoto Encyclopedia of Genes and Genomes (KEGG) ferroptosis pathway (mmu04216) in the liver of *Fbxl5*$^{F/F}$ (control) and *Alb*-Cre/*Fbxl5*$^{F/F}$ (FBXL5 liver-KO) mice at 3 hours after iron administration. Abbreviations: FDR-*q*, false discovery rate *q* value; FBXL5, F-box and leucine-rich repeat protein 5; KO, knockout; NES, normalized enrichment score.

GSEA using the iFerroptosis gene list revealed significant enrichment of hepatic ferroptosis response genes in the HIRI (Figure 3D) model ($p < 0.001$). This is consistent with previous findings showing that ferroptosis is associated with the pathogenesis of HIRI in mice.[17] In contrast, the application of the existing gene set (mmu04216) did not achieve statistical significance in the enrichment of ferroptosis-related genes in the liver transcriptomes of HIRI ($p = 0.92$). Given that mmu04216 gene set is composed of genes associated with the cellular pathway of ferroptosis induction, these results suggest that the iFerroptosis gene list, which dictates the tissue-level response to ferroptosis, may better identify the pathogenic features of ferroptosis under multiple liver pathogenesis scenarios. Notably, GSEA using the iFerroptosis gene list did not show statistically significant enrichment of hepatic ferroptosis response genes in the liver transcriptome of CCl_4-induced acute liver injury ($p = 0.97$) (Figure 3E), indicating that not all types of liver injury show enrichment of ferroptosis-related genes.

Iron overload aggravates hepatic IRI in mice

Given that GSEA using the iFerroptosis gene list suggested an association between ferroptosis and the pathogenesis of HIRI in the murine liver, we investigated whether disruption of iron homeostasis promotes ferroptosis and exacerbates HIRI. To this end, control and FBXL5 liver-KO mice were fasted for 12–16 hours, followed by 70% hepatic ischemia for 30 minutes and reperfusion for 3 hours (Figure 4A). Serum levels of AST, ALT, and LDH increased in FBXL5 liver-KO mice

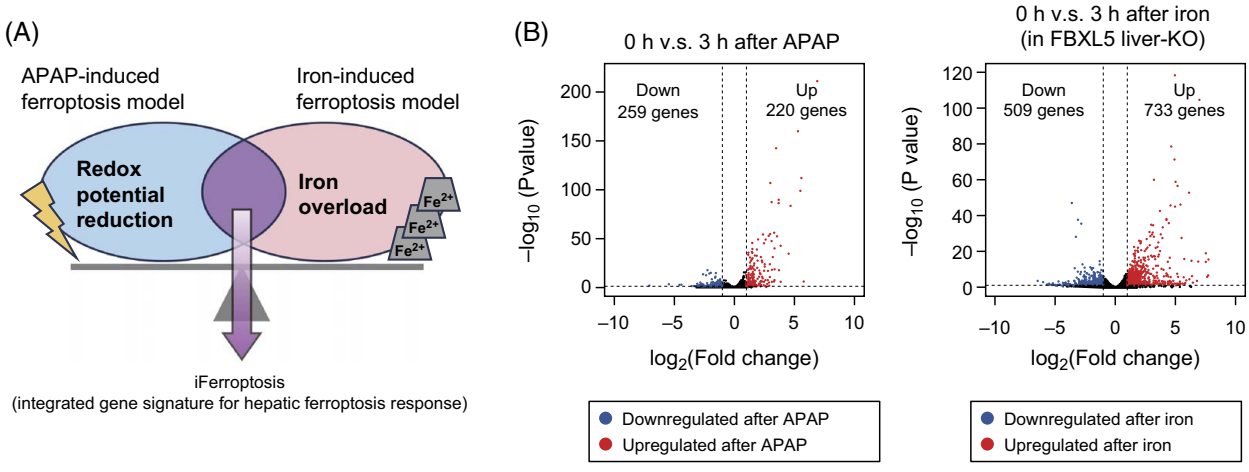

(C)

iFerroptosis

Hmox1	Serpine1	Tsc22d2	Ppp1r15a	Mdm2	Pnrc1	Zbtb21	Gm55891	Gsta1	Gcn1
Atf3	Osgin1	Btbd19	Gm3776	Cep85l	Arid5a	Txnrd1	Mthfd2	Gm12715	Cpeb2
Gdf15	Fos	Jund	Gclc	Ifrd1	Gm26759	Fosl2	Desi2	Sesn2	Sertad1
Gadd45a	Ddit3	Junb	Fbf1	Mt1	Pvr	Ppfibp2	Sqstm1	Ptp4a1	Creb3l2
Fgf21	Maff	Trib1	Junos	Zfand5	Myc	Slc35d1	Zfp36l1	Stk17b	Gm15725
Jun	Adamts1	Slc38a2	Cldn14	Gm50383	Ets2	Chd1	Foxo3	Gm17024	Ccnl1
Ier2	Klf6	Dynlt4	Dusp4	Rcan1	Gm45774	Ccdc120	Chka	Ddit4	Mafk
Chac1	Plk3	Gm7008	Epha2	Gm56727	BC005537	Eppk1	Irf2bp2	D16Ertd472e	Mt2
E230016M11Rik	Btg2	Rnd3	Gm57157	Zfp36	1700017B05Rik	Actg1	Ptp4a1	Csrnp1	Gjb2
Igfbp1	Atf4	Brd2	Gm11175	Cd14	Srrm4	Nfkbiz	Mideas	Pgd	Bach1

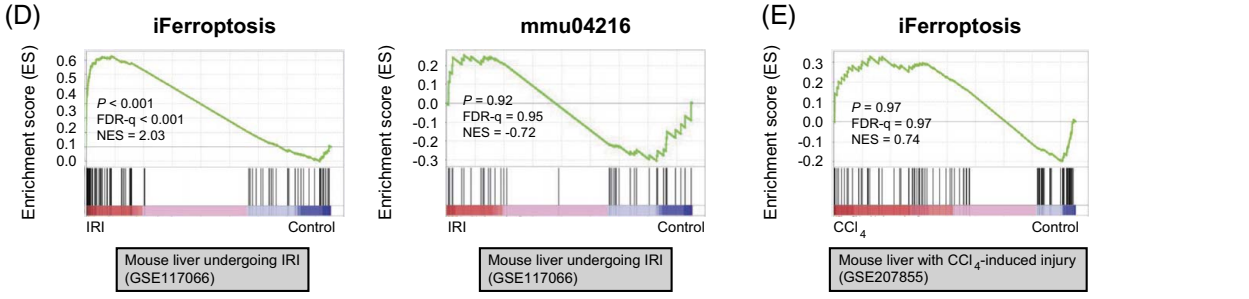

FIGURE 3 Integrated ferroptosis response gene signature dictates ferroptosis-related pathological response in mouse liver. (A) Schematic overview of the strategy for creating an integrated gene signature for hepatic ferroptosis response (iFerroptosis). (B) The left panel shows volcano plot of differentially expressed genes (DEGs; fold change >2 and adjusted $p<0.01$) in the liver of mice treated with APAP, comparing samples collected at 0 and 3 hours after intrapreneurial injection. The right panel shows DEGs in the liver of *Alb*-Cre/*Fbxl5*$^{F/F}$ (FBXL5 liver-KO) mice treated with iron, comparing samples collected at 0 and 3 hours after oral gavage injection. The genes with upregulated and downregulated expressions are shown in red and blue, respectively. RNA sequencing data for the APAP-induced ferroptosis model were obtained from Li et al.[32] (C) The top 100 genes with upregulated expressions in the iFerroptosis gene signature. (D) GSEA (gene set enrichment analysis) of the iFerroptosis gene signature (left panel) or the KEGG (Kyoto Encyclopedia of Genes and Genomes) ferroptosis pathway (mmu04216) (right panel) in the mouse liver undergoing IRI. RNA sequencing data were obtained from Zhang et al.[37] (E) GSEA of the iFerroptosis gene signature in the mouse liver with carbon tetrachloride-induced injury. RNA sequencing data were obtained from Xi et al.[34] Abbreviations: APAP, acetaminophen; FBXL5, F-box and leucine-rich repeat protein 5; FDR-*q*, false discovery rate *q* value; IRI, ischemia-reperfusion injury; KO, knockout; NES, normalized enrichment score.

after HIRI compared to those in controls, and these effects were significantly suppressed by Fer-1 treatment (Figure 4B). Consistent with these results, microscopic analysis of sections stained with 4-HNE suggested an increase in lipid peroxidation in the livers of FBXL5 liver-KO mice, which was mitigated by Fer-1 treatment (Figure 4C). These results demonstrated that iron overload in FBXL5 liver-KO mice promoted ferroptosis

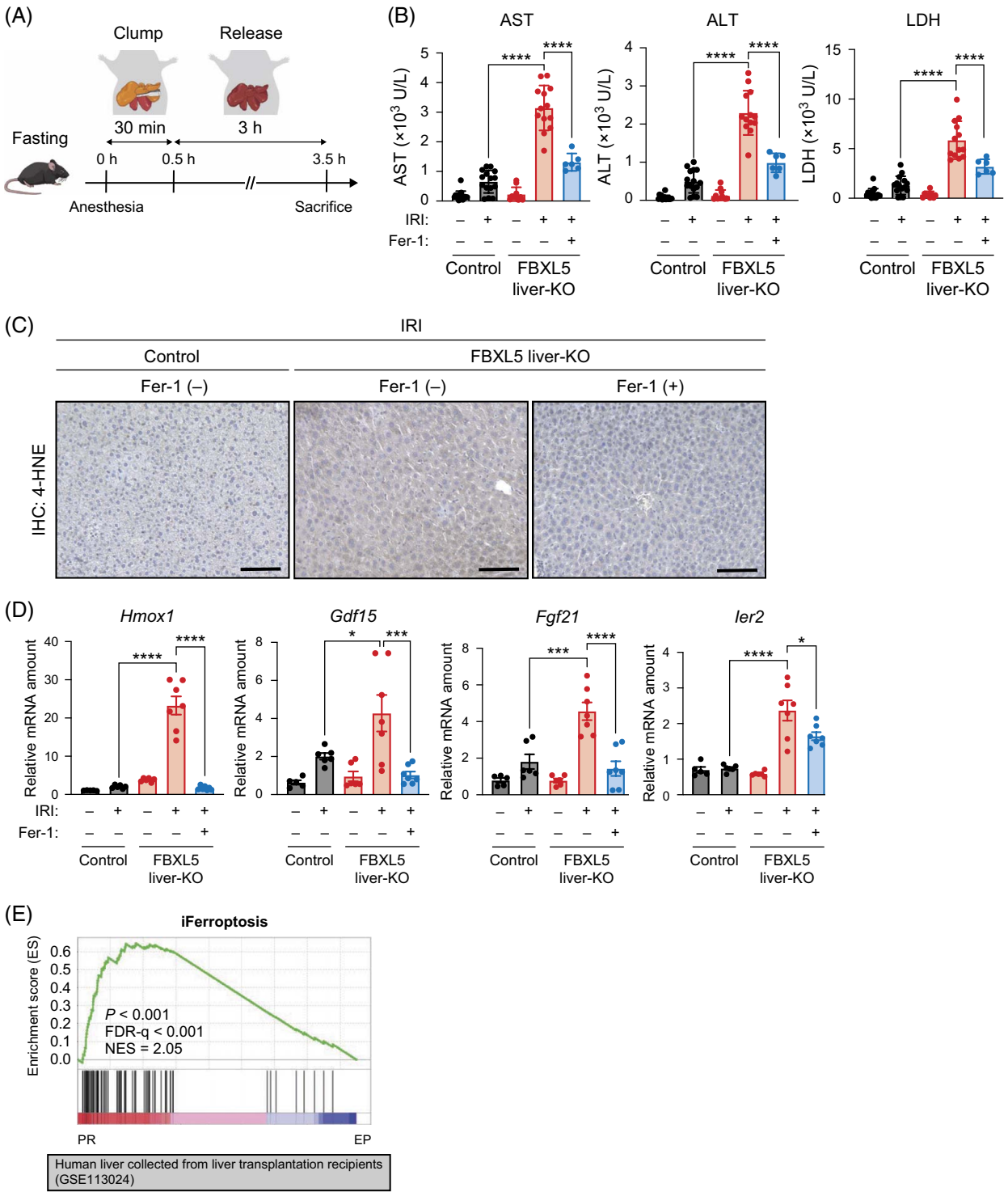

FIGURE 4 Iron overload aggravates hepatic ischemia-reperfusion injury in mice. (A) Schematic overview of the experimental procedure for the 70% IRI model. (B) Serum levels of AST, ALT, and LDH in *Fbxl5*$^{F/F}$ (control) and *Alb*-Cre/*Fbxl5*$^{F/F}$ (FBXL5 liver-KO) mice after IRI. Where indicated, FBXL5 liver-KO mice were provided (or not) with Fer-1 for 1 hour prior to IRI. Data are represented as mean ± SD. The number of mice used for this data are as follows: n = 16 and 15 mice for sham and IRI, respectively, for the control group; and n = 10, 13, 6 mice for sham, IRI, and IRI with Fer-1 treatment, respectively, for the FBXL5 liver-KO group. ****$p < 0.0001$ (one-way ANOVA test followed by the Tukey multiple comparison test). (C) IHC staining with antibodies against 4-HNE of the liver of *Fbxl5*$^{F/F}$ (control) and *Alb*-Cre/*Fbxl5*$^{F/F}$ (FBXL5 liver-KO) mice after IRI. Mice were provided (or not) with Fer-1 as described in (B). Scale bars represent 100 μm. (D) RT and real-time PCR analysis of the indicated mRNA in liver tissues of *Fbxl5*$^{F/F}$ (control) and *Alb*-Cre/*Fbxl5*$^{F/F}$ (FBXL5 liver-KO) mice after IRI. Mice were provided (or not) with Fer-1 as described in (B). The expression levels of the following genes were studied: heme oxygenase 1 (*Hmox1*); growth and differentiation factor 15 (*Gdf15*); fibroblast growth factor 21 (*Fgf21*); immediate early response 2 (*Ier2*). Data are represented as mean ± SEM. The number of mice used for this data are as follows: n = 5 and 6 mice for sham and IRI, respectively, for the control group; and n = 6, 7, and 7 mice for sham, IRI, and IRI

with Fer-1 treatment, respectively, for the FBXL5 liver-KO group. $*p < 0.05$; $***p < 0.001$; $****p < 0.0001$ (one-way ANOVA test followed by the Tukey multiple comparison test). (E) GSEA of the iFerroptosis gene signature in the transplanted human liver, comparing samples collected at the end of preservation and 1 hour post-graft revascularization during conventional liver transplantation. RNA sequencing data were obtained from Guo et al.[35] Abbreviations: 4-HNE, 4-hydroxynonenal; FBXL5, F-box and leucine-rich repeat protein 5; FDR-*q*, false discovery rate *q* value; IHC, immunohistochemical; IRI, ischemia-reperfusion injury; KO, knockout; LDH, lactate dehydrogenase; NES, normalized enrichment score.

during HIRI, leading to severe liver damage. We next validated the iFerroptosis gene signature in this context by individually evaluating the expression of several iFerroptosis genes for which PCR primer sets were available, including heme oxygenase 1 (*Hmox1*), growth differentiation factor 15 (*Gdf15*), fibroblast growth factor 21 (*Fgf21*), and immediate early response 2 (*Ier2*) (Figure 4D). Reverse transcription (RT) and quantitative PCR analyses revealed that the expression of these genes was substantially upregulated under HIRI in the livers of *Fbxl5* liver-KO mice, which was reduced by Fer-1 treatment (Figure 4D). These results suggest that the expression levels of iFerroptosis genes are associated with the induction of ferroptosis during HIRI in mice, prompting us to apply this list to the human HIRI transcriptome. Although our validation of the iFerroptosis gene list was conducted using the warm HIRI model, in which livers were kept warm during ischemia and reperfusion, we found that human livers undergoing cold HIRI during conventional liver transplantation (Supplemental Table S8, http://links.lww.com/HC9/B992)[35] also displayed significant enrichment of hepatic ferroptosis response genes ($p < 0.001$) (Figure 4E). These results suggest that ferroptosis is associated with the pathogenesis of both warm and cold HIRI. Additionally, our data indicate the potential of the iFerroptosis gene list to predict ferroptosis-associated pathogenesis in both human and mouse livers.

Patients with high-iron status show sustained postoperative liver damage

Our data suggest that iron aggravates HIRI. HIRI is often a problem not only in liver transplantation but also in liver resection surgery.[19,38] The Pringle maneuver method, used to prevent bleeding during liver resection, causes temporary ischemia and subsequent reperfusion of the liver.[39,40] Therefore, we investigated the impact of iron and ferroptosis on recovery from warm HIRI caused by hepatectomy in humans. Preoperative serum iron levels were measured in 174 of 1014 liver resections performed for HCC at Kumamoto University between 2007 and 2023, where the Pringle maneuver method was used to prevent intraoperative hemorrhage. These 174 cases were divided into 2 groups based on preoperative serum iron levels (cutoff value: 150 μg/dL): a low-iron group (n = 143) and a high-iron group (n = 31) (Figure 5A and Table 1). This criterion allowed these groups to be further divided according to serum iron levels, with AST and ALT levels increasing in the high-serum iron group (Figure 5B). These results suggest that elevated iron levels in patients with HCC are associated with increased liver damage. In contrast, there was no significant difference in albumin levels and indocyanine green retention 15 (ICG-R15) values between the low-iron and high-iron groups, which were used to evaluate resectability for hepatectomy (Table 1). Additionally, there was no significant difference in the duration of the Pringle maneuver between the 2 groups, suggesting that the amount of ischemia-reperfusion stress was comparable in both groups (Figure 5B).

To investigate the mechanisms underlying the higher preoperative transaminase levels in the high-iron group than in the low-iron group, we collected 3 liver samples from each group and examined the gene expression profiles of non-cancerous background regions of the liver (Figure 5C and Supplemental Table S9, http://links.lww.com/HC9/B993). GSEA using the iFerroptosis gene list revealed a significant enrichment of the hepatic ferroptosis response in patients with a high-iron status compared to those with a low-iron status (Figure 5D). Histological analysis revealed extensive accumulation of iron (Figure 5E) and lipid peroxidation (Figure 5F) in the high-iron group. These observations suggest that patients with high-serum iron levels accumulate iron in the liver, thereby increasing the susceptibility of hepatocytes to ferroptosis and resulting in liver damage. Next, we investigated the impact of iron accumulation on recovery from hepatectomy-induced HIRI. The serum levels of AST and ALT were high and showed no statistical difference between the low-iron and high-iron groups 1 day after surgery, possibly reflecting massive liver destruction because of hepatectomy (Figure 5G). This increase in serum transaminase levels gradually decreased over time in the low-iron group, as evident from the AST and ALT levels on postoperative days 3 and 5 (Figures 5G, H). In contrast, patients with high-iron status showed delayed recovery from hepatectomy, with a significant difference in the serum levels of AST and ALT between the low-iron and high-iron groups (Figures 5G, H). Therefore, our data indicate that patients with high-iron levels accumulate iron in the liver, disrupting the prompt recovery from HIRI by increasing the susceptibility of hepatocytes to ferroptosis.

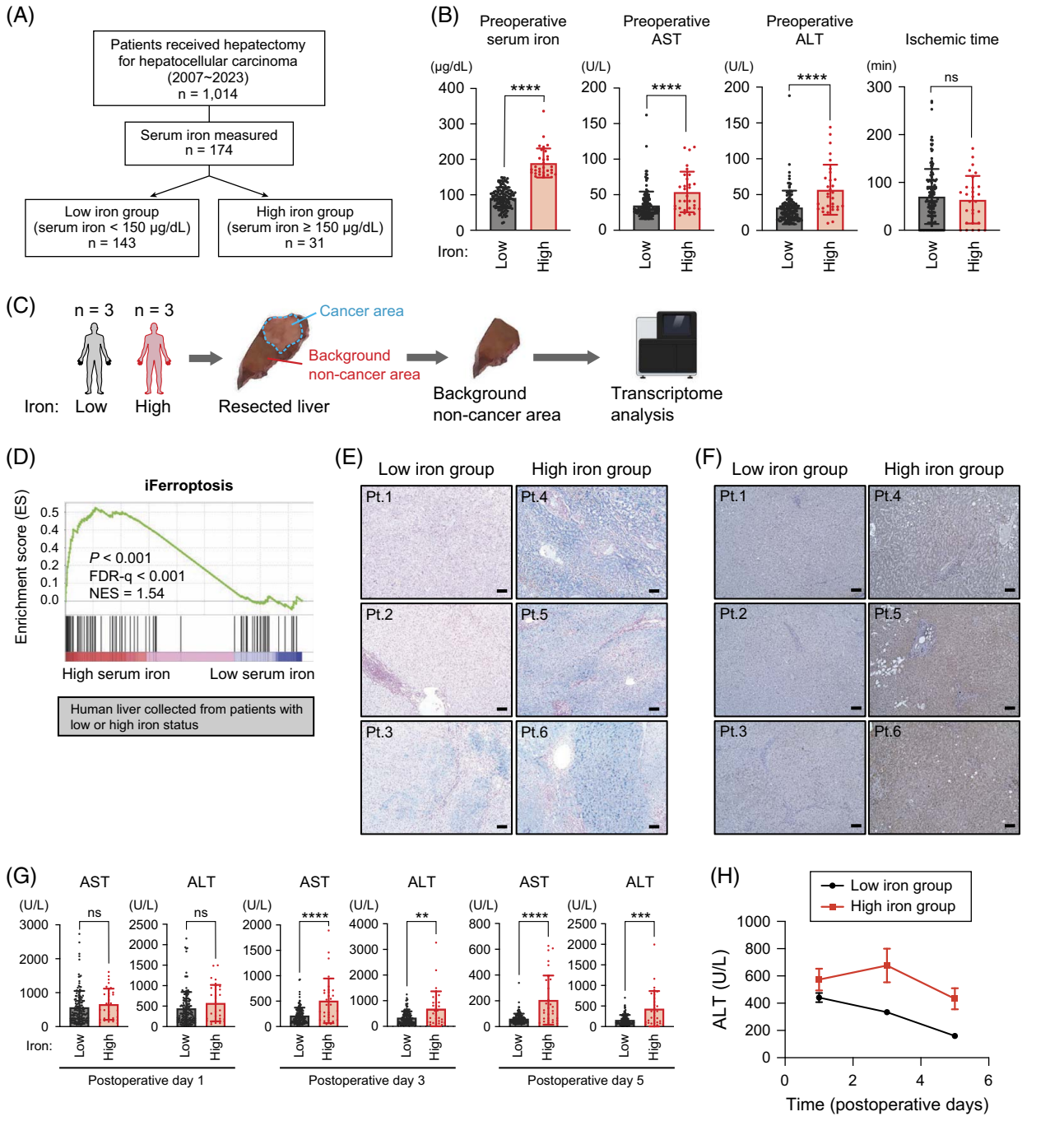

FIGURE 5 Patients with high-iron status show sustained postoperative liver damage. (A) Schematic flow chart of clinical sample collection. (B) Preoperative serum levels of iron, AST, and ALT, as well as ischemic time during operation, in patients with HCC with low-iron or high-iron status. Data are represented as mean ± SD. The number of patients are as follows: serum levels of iron, AST, and ALT, n = 143 and 31 patients for the low-iron and high-iron group, respectively; ischemic time, n = 138 and 28 patients for the low-iron and high-iron group, respectively. ns, not significant ($p > 0.05$); ****$p < 0.0001$ (Mann–Whitney *U* test). (C) Schematic overview of patient sample preparation for the transcriptome analysis. (D) GSEA (gene set enrichment analysis) of the iFerroptosis gene signature in the resected human liver, comparing samples collected from patients with low-iron and high-iron status. (E and F) Histological analysis of resected non-cancerous human liver. The Perls Prussian blue staining for the detection of iron is shown in (E), and IHC staining with antibodies against 4-HNE is shown in (F). Scale bars represent 100 μm. (G) Serum levels of AST and ALT in patients with HCC with low-iron or high-iron status at the indicated times after hepatectomy. Data are represented as mean ± SD; n = 143 and 31 patients for the low-iron and high-iron groups, respectively. ns, not significant ($p > 0.05$); **$p < 0.01$; ***$p < 0.001$; ****$p < 0.0001$ (Mann–Whitney *U* test). (H) The time course of changes in serum ALT levels in patients, as described in (G), is represented as mean ± SEM data. Abbreviations: FDR-*q*, false discovery rate *q* value; NES, normalized enrichment score.

TABLE 1 Association between serum iron levels and clinicopathological factors in patients with HCC

	Low iron < 150 μg/dL (n = 143)	High iron ≥ 150 μg/dL (n = 31)	*p*
Age	69.7 ± 9.4	66.3 ± 11.2	0.10
Sex (M/F)	102/41	24/7	0.41
BMI (kg/m^2)	23.5 ± 2.1	24.2 ± 2.7	0.31
HBs-Ag (+)	31 (22%)	4 (13%)	0.38
HCV-Ab (+)	59 (41%)	20 (65%)	0.03
Albumin (g/dL)	4.1 ± 0.4	4.0 ± 0.4	0.74
AST (IU/L)	36.9 ± 21	56.0 ± 28	< 0.001
ALT (IU/L)	34.5 ± 25	61.3 ± 35	< 0.001
CRP (mg/dL)	0.14 ± 0.40	0.084 ± 0.08	0.46
ICG-R15 min (%)	13.0 ± 7.1	13.3 ± 7.6	0.81
Prothrombin activity (%)	96 ± 19	97 ± 24	0.82
Plt (10^4/μL)	18.2 ± 18.3	14.3 ± 3.9	0.26
Tumor size (mm)	27.5 ± 11.8	24.3 ± 8.3	0.18
Tumor number	1 (1–3)	1 (1–3)	0.35
AFP (mAU/mL)	905 ± 3804	126 ± 373	0.28
AFP-L3 (%)	12 ± 21.5	7.7 ± 12.4	0.32
PIVKA-II (mAU/mL)	189 ± 450	335 ± 831	0.21
Operation time (min)	373 ± 110	398 ± 97	0.29
Blood loss (mL)	457 ± 440	378 ± 323	0.37
Ischemic time (min)	71 ± 58	64 ± 50	0.56
Laparoscopic resection	50 (35%)	12 (39%)	0.67
Anatomic resection	81 (57%)	18 (58%)	0.97

Abbreviations: AFP, α-fetoprotein; AFP-L3, Lens culinaris agglutinin-A-reactive α-fetoprotein; BMI, body mass index; CRP, C-reactive protein; ICG-R15 min, indocyanine retention rate at 15 minutes; PIVKA-II, protein induced by vitamin K absence or antagonist-II; Plt, platelet count; PT, prothrombin time.

DISCUSSION

Identifying and characterizing ferroptosis-related pathogenesis in liver disease using bulk RNA sequencing data has posed challenges for several reasons. These include context-dependent involvement of ferroptosis-related molecules and the lack of a consistent gene set capable of reliably identifying a ferroptosis signature in vivo. In the present study, we developed a hepatic ferroptosis response gene set (iFerroptosis) comprising 100 genes whose expressions are commonly upregulated in iron-induced and APAP-induced ferroptosis models. Validation was conducted in murine models of HIRI, as well as in human liver samples obtained during resections for HCC. To construct this gene set, we established a novel mouse model of iron overload-induced ferroptosis using liver-specific *Fbxl5* knockout mice. Using publicly available RNA sequencing data, we demonstrated the applicability of the iFerroptosis gene set in both murine and human contexts, emphasizing the pivotal role of iron and ferroptosis in ischemic liver injury. The proposed iFerroptosis gene signature encompasses transcriptional profiles not only from hepatocytes but also from other cells involved in tissue responses, including cholangiocytes, stellate cells, endothelial cells, Kupffer cells, and immune cells. This contrasts with the existing ferroptosis-related gene set (mmu04216), which comprises genes associated with the cellular pathways involved in ferroptosis induction. Notably, our iFerroptosis gene signature does not include genes known for their critical roles in ferroptosis induction, such as *GPX4* and acyl-CoA synthetase long-chain family member 4 (*ACSL4*).[4] Pathway gene sets, such as mmu04216, typically compile genes linked to the pathway from individual studies or large-scale analyses. Although these pathway gene lists may capture events that could be associated with ferroptosis under certain conditions, the complex response of the liver to ferroptosis in vivo suggests that our newly constructed gene list may more accurately depict ferroptosis features in multiple liver pathogenesis scenarios. However, this study exclusively focused on hepatic responses to ferroptosis; thus, it is uncertain whether the iFerroptosis gene set is applicable across other tissues. Future studies could extend this experimental approach by generating tissue-specific *Fbxl5* knockout mice in other organs, such as the kidneys and heart, and developing gene signatures that describe tissue-specific responses to iron-induced ferroptosis.

Liver resection is the optimal curative treatment for hepatobiliary malignancies, such as liver cancer. For decades, the Child–Pugh score has been utilized to assess liver function. This assessment incorporates specific blood markers, such as serum bilirubin, albumin, and prothrombin levels, along with clinical observations, including the presence of hepatic encephalopathy and ascites.[41] In recent years, the utility of the ALBI (albumin–bilirubin) score, which uses albumin and bilirubin levels, has been reported. Additionally, the indocyanine green retention rate at 15 minutes (ICG-R15), which measures indocyanine green, has been reported to correlate with liver reserve function as an assessment parameter.[42] In the present study, we demonstrated that preoperative serum iron levels are associated with perioperative liver damage in patients with HCC. Therefore, incorporating the preoperative serum iron status into these scoring criteria could be beneficial for preventing postoperative complications and liver failure. Our findings demonstrate that iron overload induced by the liver-specific deletion of *Fbxl5* aggravates HIRI in mice, suggesting that strict control of hepatic iron status is crucial for managing HIRI. As HIRI is a notable clinical problem, especially following liver transplantation and major resection,[43,44] targeting iron in the liver may be a

promising strategy for mitigating HIRI and improving liver surgery outcomes.

In conclusion, our study identified a gene signature indicative of hepatic ferroptosis in both mice and humans. Utilizing the iFerroptosis gene set may help to further understand ferroptosis-related hepatic disorders and offer insights into potential therapeutic strategies targeting ferroptosis to improve outcomes in patients with liver diseases.

DATA AVAILABILITY STATEMENT

The RNA-seq data generated in this study have been deposited in the DNA Data Bank of Japan (DDBJ) at PRJDB18097 and PRJDB18207. All other raw data generated in this study are available from the corresponding author upon request.

AUTHOR CONTRIBUTIONS

Study concept and design: Takashi Matsumoto and Toshiro Moroishi. Acquisition of data: Takashi Matsumoto, Akihiro Nita, Tomomi Nita, Yohei Kanamori, Ayato Maeda, Noriko Yasuda-Yoshihara, Kosuke Mima, Yuta Matsuoka, and Katsuya Nagaoka. Analysis and interpretation of data: Takashi Matsumoto, Akihiro Nita, Noriko Yasuda-Yoshihara, Hirohisa Okabe, Katsunori Imai, Yuta Matsuoka, Yuki Sugiura, and Toshiro Moroishi. Drafting of the manuscript: Takashi Matsumoto, Akihiro Nita, and Toshiro Moroishi. Critical revision of the manuscript for important intellectual content: Takashi Matsumoto, Akihiro Nita, Hiromitsu Hayashi, Keiichi I. Nakayama, Yasuhito Tanaka, Hideo Baba, and Toshiro Moroishi. Statistical analysis: Takashi Matsumoto, Akihiro Nita, and Toshiro Moroishi. Study supervision; Yuki Sugiura, Yasuhito Tanaka, Hideo Baba, and Toshiro Moroishi.

FUNDING INFORMATION

This study was supported by Japan Society for the Promotion of Science (JSPS) KAKENHI grants (23K18098, 24H00864, and 24H00865 to Toshiro Moroishi), Japan Science and Technology Agency (JST) FOREST Program (JPMJFR226J to Toshiro Moroishi), Kobayashi Foundation for Cancer Research (to Toshiro Moroishi), Princess Takamatsu Cancer Research Fund (to Toshiro Moroishi), Ichiro Kanehara Foundation (to Toshiro Moroishi), Foundation for Promotion of Cancer Research in Japan (to Toshiro Moroishi), Kato Memorial Bioscience Foundation (to Toshiro Moroishi), Japan Agency for Medical Research and Development (AMED; JP23fk0210103 to Yasuhito Tanaka), and Collaborative Research Grant from Center for Metabolic Regulation of Healthy Aging (CMHA; to Yasuhito Tanaka).

ACKNOWLEDGMENTS

This study was supported by Japan Society for the Promotion of Science (JSPS) KAKENHI grants (23K18098, 24H00864, and 24H00865 to Toshiro Moroishi), Japan Science and Technology Agency (JST) FOREST Program (JPMJFR226J to Toshiro Moroishi), Kobayashi Foundation for Cancer Research (to Toshiro Moroishi), Princess Takamatsu Cancer Research Fund (to Toshiro Moroishi), Ichiro Kanehara Foundation (to Toshiro Moroishi), Foundation for Promotion of Cancer Research in Japan (to Toshiro Moroishi), Kato Memorial Bioscience Foundation (to Toshiro Moroishi), Japan Agency for Medical Research and Development (AMED; JP23fk0210103 to Yasuhito Tanaka), and Collaborative Research Grant from Center for Metabolic Regulation of Healthy Aging (CMHA; to Yasuhito Tanaka). The authors thank the Core Laboratory for Medical Research and Education, Kumamoto University School of Medicine, for their technical support.

CONFLICTS OF INTEREST

Noriko Yasuda-Yoshihara consults, advises, and is employed by GAIA BioMedicine Incorporated. The remaining authors have no conflicts to report.

ORCID

Takashi Matsumoto https://orcid.org/0000–0001–6791–6441
Akihiro Nita https://orcid.org/0000–0003–2647–5445
Yohei Kanamori https://orcid.org/0009–0003–4062–5910
Noriko Yasuda-Yoshihara https://orcid.org/0000–0001–9550–3257
Kosuke Mima https://orcid.org/0000–0002–4385–4984
Hirohisa Okabe https://orcid.org/0000–0003–3041–7563
Katsunori Imai https://orcid.org/0000–0003–0549–1825
Hiromitsu Hayashi https://orcid.org/0000–0002–1832–4287
Yuta Matsuoka https://orcid.org/0000–0001–9860–3851
Katsuya Nagaoka https://orcid.org/0000–0002–7152–6101
Keiichi I. Nakayama https://orcid.org/0000–0002–7185–1529
Yuki Sugiura https://orcid.org/0000–0002–6983–8958
Yasuhito Tanaka https://orcid.org/0000–0002–2473–6966
Hideo Baba https://orcid.org/0000–0002–3474–2550
Toshiro Moroishi https://orcid.org/0000–0001–6419–3882

REFERENCES

1. Li J, Cao F, Yin H, Huang Z, Lin Z, Mao N, et al. Ferroptosis: Past, present and future. Cell Death Dis. 2020;11:88.
2. Stockwell BR. Ferroptosis turns 10: Emerging mechanisms, physiological functions, and therapeutic applications. Cell. 2022; 185:2401–21.

3. Dixon SJ, Lemberg KM, Lamprecht MR, Skouta R, Zaitsev EM, Gleason CE, et al. Ferroptosis: An iron-dependent form of nonapoptotic cell death. Cell. 2012;149:1060–72.
4. Jiang X, Stockwell BR, Conrad M. Ferroptosis: Mechanisms, biology and role in disease. Nat Rev Mol Cell Biol. 2021;22: 266–82.
5. Zheng H, Jiang L, Tsuduki T, Conrad M, Toyokuni S. Embryonal erythropoiesis and aging exploit ferroptosis. Redox Biol. 2021; 48:102175.
6. Mazhar M, Din AU, Ali H, Yang G, Ren W, Wang L, et al. Implication of ferroptosis in aging. Cell Death Discov. 2021;7:149.
7. Belaidi AA, Bush AI. Iron neurochemistry in Alzheimer's disease and Parkinson's disease: Targets for therapeutics. J Neurochem. 2016;139(suppl 1):179–97.
8. Southon A, Szostak K, Acevedo KM, Dent KA, Volitakis I, Belaidi AA, et al. Cu(II) (atsm) inhibits ferroptosis: Implications for treatment of neurodegenerative disease. Br J Pharmacol. 2020; 177:656–67.
9. Chen L, Na R, Danae McLane K, Thompson CS, Gao J, Wang X, et al. Overexpression of ferroptosis defense enzyme Gpx4 retards motor neuron disease of SOD1G93A mice. Sci Rep. 2021;11:12890.
10. Yamane D, Hayashi Y, Matsumoto M, Nakanishi H, Imagawa H, Kohara M, et al. FADS2-dependent fatty acid desaturation dictates cellular sensitivity to ferroptosis and permissiveness for hepatitis C virus replication. Cell Chem Biol. 2022;29: 799–810.e4.
11. Bednash JS, Kagan VE, Englert JA, Farkas D, Tyurina YY, Tyurin VA, et al. Syrian hamsters as a model of lung injury with SARS-CoV-2 infection: Pathologic, physiologic, and detailed molecular profiling. Transl Res. 2022;240:1–16.
12. Li P, Jiang M, Li K, Li H, Zhou Y, Xiao X, et al. Glutathione peroxidase 4-regulated neutrophil ferroptosis induces systemic autoimmunity. Nat Immunol. 2021;22:1107–17.
13. Nagasaki T, Schuyler AJ, Zhao J, Samovich SN, Yamada K, Deng Y, et al. 15LO1 dictates glutathione redox changes in asthmatic airway epithelium to worsen type 2 inflammation. J Clin Invest. 2022;132:e151685.
14. Toyokuni S, Ito F, Yamashita K, Okazaki Y, Akatsuka S. Iron and thiol redox signaling in cancer: An exquisite balance to escape ferroptosis. Free Radic Biol Med. 2017;108:610–26.
15. Ubellacker JM, Tasdogan A, Ramesh V, Shen B, Mitchell EC, Martin-Sandoval MS, et al. Lymph protects metastasizing melanoma cells from ferroptosis. Nature. 2020;585:113–8.
16. Wu W, Li D, Feng X, Zhao F, Li C, Zheng S, et al. A pan-cancer study of selenoprotein genes as promising targets for cancer therapy. BMC Med Genomics. 2021;14:78.
17. Chen J, Li X, Ge C, Min J, Wang F. The multifaceted role of ferroptosis in liver disease. Cell Death Differ. 2022;29: 467–80.
18. Li R, Yan X, Xiao C, Wang T, Li X, Hu Z, et al. FTO deficiency in older livers exacerbates ferroptosis during ischaemia/reperfusion injury by upregulating ACSL4 and TFRC. Nat Commun. 2024;15:4760.
19. Zhai Y, Petrowsky H, Hong JC, Busuttil RW, Kupiec-Weglinski JW. Ischaemia-reperfusion injury in liver transplantation—From bench to bedside. Nat Rev Gastroenterol Hepatol. 2013;10: 79–89.
20. Jaeschke H. Reactive oxygen and mechanisms of inflammatory liver injury: Present concepts. J Gastroenterol Hepatol. 2011;26 (suppl 1):173–9.
21. Bayır H, Anthonymuthu TS, Tyurina YY, Patel SJ, Amoscato AA, Lamade AM, et al. Achieving life through death: Redox biology of lipid peroxidation in ferroptosis. Cell Chem Biol. 2020;27: 387–408.
22. Yamada N, Karasawa T, Kimura H, Watanabe S, Komada T, Kamata R, et al. Ferroptosis driven by radical oxidation of n-6 polyunsaturated fatty acids mediates acetaminophen-induced acute liver failure. Cell Death Dis. 2020;11:144.
23. Seiler A, Schneider M, Förster H, Roth S, Wirth EK, Culmsee C, et al. Glutathione peroxidase 4 senses and translates oxidative stress into 12/15-lipoxygenase dependent- and AIF-mediated cell death. Cell Metab. 2008;8:237–48.
24. Maio N, Zhang DL, Ghosh MC, Jain A, SantaMaria AM, Rouault TA. Mechanisms of cellular iron sensing, regulation of erythropoiesis and mitochondrial iron utilization. Semin Hematol. 2021;58:161–74.
25. Muckenthaler MU, Rivella S, Hentze MW, Galy B. A red carpet for iron metabolism. Cell. 2017;168:344–61.
26. Galy B, Conrad M, Muckenthaler M. Mechanisms controlling cellular and systemic iron homeostasis. Nat Rev Mol Cell Biol. 2024;25:133–55.
27. Moroishi T, Nishiyama M, Takeda Y, Iwai K, Nakayama KI. The FBXL5–IRP2 axis is integral to control of iron metabolism in vivo. Cell Metab. 2011;14:339–51.
28. Salahudeen AA, Thompson JW, Ruiz JC, Ma HW, Kinch LN, Li Q, et al. An E3 ligase possessing an iron-responsive hemerythrin domain is a regulator of iron homeostasis. Science. 2009;326: 722–6.
29. Vashisht AA, Zumbrennen KB, Huang X, Powers DN, Durazo A, Sun D, et al. Control of iron homeostasis by an iron-regulated ubiquitin ligase. Science. 2009;326:718–21.
30. Postic C, Magnuson MA. DNA excision in liver by an albumin-Cre transgene occurs progressively with age. Genesis. 2000;26: 149–50.
31. Matsuoka Y, Takahashi M, Sugiura Y, Izumi Y, Nishiyama K, Nishida M, et al. Structural library and visualization of endogenously oxidized phosphatidylcholines using mass spectrometry-based techniques. Nat Commun. 2021; 12:6339.
32. Li C, Ming Y, Hong W, Tang Y, Lei X, Li X, et al. Comparison of hepatic transcriptome profiling between acute liver injury and acute liver failure induced by acetaminophen in mice. Toxicol Lett. 2018;283:69–76.
33. Li X, Wang TX, Huang X, Li Y, Sun T, Zang S, et al. Targeting ferroptosis alleviates methionine-choline deficient (MCD)-diet induced NASH by suppressing liver lipotoxicity. Liver Int. 2020; 40:1378–94.
34. Xi Y, LaCanna R, Ma HY, N'Diaye EN, Gierke S, Caplazi P, et al. A WISP1 antibody inhibits MRTF signaling to prevent the progression of established liver fibrosis. Cell Metab. 2022;34: 1377–393.e8.
35. Guo Z, Xu J, Huang S, Yin M, Zhao Q, Ju W, et al. Abrogation of graft ischemia-reperfusion injury in ischemia-free liver transplantation. Clin Transl Med. 2022;12:e546.
36. Kagan VE, Mao G, Qu F, Angeli JPF, Doll S, Croix CS, et al. Oxidized arachidonic and adrenic PEs navigate cells to ferroptosis. Nat Chem Biol. 2017;13:81–90.
37. Zhang P, Ming Y, Cheng K, Niu Y, Ye Q. Gene expression profiling in ischemic postconditioning to alleviate mouse liver ischemia/reperfusion injury. Int J Med Sci. 2019;16: 343–54.
38. Cannistrà M, Ruggiero M, Zullo A, Gallelli G, Serafini S, Maria M, et al. Hepatic ischemia reperfusion injury: A systematic review of literature and the role of current drugs and biomarkers. Int J Surg. 2016;33(suppl 1):S57–70.
39. Pringle JH. Notes on the arrest of hepatic hemorrhage due to trauma. Ann Surg. 1908;48:541–9.
40. Huguet C, Addario-Chieco P, Gavelli A, Arrigo E, Harb J, Clement RR. Technique of hepatic vascular exclusion for extensive liver resection. Am J Surg. 1992;163:602–5.
41. Child CG, Turcotte JG. Surgery and portal hypertension. Major Probl Clin Surg. 1964;1:1–85.
42. Johnson PJ, Berhane S, Kagebayashi C, Satomura S, Teng M, Reeves HL, et al. Assessment of liver function in patients with hepatocellular carcinoma: A new evidence-based approach—The ALBI grade. J Clin Oncol. 2015;33:550–8.

43. Duffy JP, Kao K, Ko CY, Farmer DG, McDiarmid SV, Hong JC, et al. Long-term patient outcome and quality of life after liver transplantation: Analysis of 20-year survivors. Ann Surg. 2010; 252:652–61.
44. Liu Y, Lu T, Zhang C, Xu J, Xue Z, Busuttil RW, et al. Activation of YAP attenuates hepatic damage and fibrosis in liver ischemia-reperfusion injury. J Hepatol. 2019;71: 719–30.

How to cite this article: Matsumoto T, Nita A, Kanamori Y, Maeda A, Nita T, Yasuda-Yoshihara N, et al. Integrated hepatic ferroptosis gene signature dictates pathogenic features of ferroptosis. Hepatol Commun. 2025;9:e0721. https://doi.org/10.1097/HC9.0000000000000721